Protons in Oxysulfides, Oxysulfates and Sulfides: A First-Principles Study of La_2O_2S, $La_2O_2SO_4$, $SrZrS_3$ and $BaZrS_3$

Jonathan M. Polfus[a*], Truls Norby[b], Rune Bredesen[a]

[a]SINTEF Materials and Chemistry, Sustainable Energy Technology, Forskningsveien 1, NO-0314 Oslo, Norway
[b]Department of Chemistry, University of Oslo, Centre for Materials Science and Nanotechnology (SMN), FASE, Gaustadalléen 21, NO-0349 Oslo, Norway

*Contact email: jonathan.polfus@sintef.no

Abstract
Sulfur-containing materials may be of importance in devices such as proton conducting fuel cells for energy conversion involving fossil or bio-derived fuels. First-principles calculations were employed to elucidate the thermodynamics of proton incorporation as well as proton migration barriers in selected sulfides, oxysulfides and oxysulfates. In this respect, dissolution of H_2S and H_2O into anion vacancies as SH^- and OH^-, respectively, was considered for La_2O_2S, $La_2O_2SO_4$, and the perovskite sulfides $SrZrS_3$ and $BaZrS_3$. The structurally equivalent A-La_2O_3 and $SrZrO_3$ were included for comparison. Protons were found to be most stable associated with oxide ions as OH^- rather than with the sulfide or sulfate anions in La_2O_2S and $La_2O_2SO_4$, respectively. The enthalpies of dissolution of H_2O were calculated to -1.31 and -1.21 eV, respectively. However, the low symmetry of the protonated structures implied insubstantial long-range proton transport. $SrZrS_3$ and $BaZrS_3$ both exhibit exothermic enthalpies of dissolution of H_2S, -0.86 and -0.58 eV, respectively, which is comparable to dissolution of H_2O in several perovskite oxide proton conductors. Furthermore, among the calculated proton migration barriers for an interoctahedral and a rotational pathway in the perovskite sulfides and oxide, $BaZrS_3$ showed the lowest activation energy for proton transport, 0.25 eV.

Keywords: oxysulfide; oxysulfate; perovskite sulfide; protons; hydration; DFT; NEB;

1. Introduction
Proton conducting ceramics constitute an important class of materials with novel applications in electrochemical energy conversion devices such as fuel cells, electrolyzers and hydrogen permeable membranes for gas separation and catalytic membrane reactors. One of the most significant advantages of ceramic fuel cells over those based on polymer electrolytes is their compatibility with alternative fuels and the high operating temperature facilitating reforming of hydrocarbons to H_2 and CO on the electrode catalyst.[1]

Biogas and natural gas are attractive fuels for use in ceramic fuel cells, but their H_2S content – typically 1-10000 ppm in various feedstocks – poses significant challenges due to chemical stability of the ceramic components and many catalysts as well as poisoning of the electrodes. Hydrogen separation membranes for hydrogen production via steam methane reforming are similarly challenged by the presence of H_2S. Extensive efforts have been devoted to optimizing the electrolyte and electrode composition in order to increase H_2S tolerance, which is often limited to a few ppm.[2,3] Another approach is to utilize novel sulfur containing ceramic components that are thermodynamically stable at higher H_2S

concentrations. These can then be considered also for use in electrochemical oxidation of H_2S as a fuel and as a byproduct from fossil fuel refining.[4]

Evaluating ceramic sulfides as proton conducting materials is also of fundamental interest considering that hydrogen generally dissolves into ceramic oxides as protons associated with an oxide ion. The defect species can then be described as hydroxide, $OH_O^\bullet$ in Kröger-Vink[5] notation, and the equivalent defect in sulfide materials would be $SH_S^\bullet$. The stability of protons in an acceptor-doped oxide can be evaluated from the enthalpy of hydration, i.e., dissolution of water according to

$$H_2O(g) + v_O^{\bullet\bullet} + O_O^\times = 2OH_O^\bullet \tag{1}$$

where $v_O^{\bullet\bullet}$ denotes a fully ionized oxygen vacancy and $O_O^\times$ denotes a lattice oxide ion. The hydration enthalpy describes the relative stability of oxygen vacancies and protons in an oxide. An analogous reaction for a sulfide can be formulated according to dissolution of H_2S into sulfur vacancies, $v_S^{\bullet\bullet}$,

$$H_2S(g) + v_S^{\bullet\bullet} + S_S^\times = 2SH_S^\bullet \tag{2}$$

Oxysulfides are particularly enticing since stability of protons associated with both oxide and sulfide ions can be evaluated within the same structural and chemical environment. Protons and anion vacancies may be energetically preferred on different sites, leading to a combination of Eqs. 1 and 2. The thermodynamics of proton incorporation into perovskite nitrides and oxynitrides have also been investigated in a similar study; it was found that protons were preferentially associated with nitride ions in $SrTa_2O_2N$, and that the concentration of protons was significantly lower in $ThTaN_3$ compared to isostructural $SrZrO_3$.[6]

Ceramic sulfates represent distinctly different sulfur containing materials where protons can associate with oxide ions in SO_4-groups. Several phosphates such as $LaPO_4$ dissolve significant amounts of protons when acceptor doped and exhibit appreciable proton conductivities.[7–11] For sulfate materials, phosphorous can be considered as an anion acceptor dopant when substituting for sulfur, and in terms of the entire anion group this would be denoted $PO_{4\,SO_4}^{\prime}$. The binding energy of the proton to the PO_4-acceptor should then be considered. To our knowledge, phosphate acceptors in ceramic sulfates and the resulting charge compensating defects and its association to the dopant have not been considered in the literature. There are solid acids in the $CsHSO_4$–CsH_2PO_4 system where fast proton transport is reported to proceed via both SO_4 and PO_4 groups in the superprotonic state, but this represents an already fully protonated and disordered case, where the effect of the solid solution is different from that of doping.[12–14]

In the present work, we investigate the incorporation and migration of protons in selected oxysulfides, oxysulfates and sulfides. The enthalpies of the reactions in Eqs. 1 and/or 2 are evaluated for La_2O_2S, $La_2O_2SO_4$ and the orthorhombic perovskite sulfides $SrZrS_3$ and $BaZrS_3$. A-type La_2O_3 and $SrZrO_3$ are considered for comparison as they are isostructural to La_2O_2S and the perovskite sulfides, respectively. Furthermore, the activation barrier for proton migration is evaluated for selected paths in the perovskite materials. As such, the difference in activation energy can be evaluated for oxides and sulfides in the same structural environment. The combination of first-principles methods and thermodynamic models is demonstrated as an effective approach to elucidate central parts of the defect chemistry and defect-dependent properties of the considered materials, in particular for the compositions with multiple anions.

2. Computational procedure

DFT calculations were performed using the projector-augmented wave (PAW) method[15,16] as implemented in VASP[17–19] and the generalized gradient approximation by Perdew, Burke and Ernzerhof (GGA-PBE).[20] Geometric optimization of the unit cells was performed with a plane wave cut-off energy of 450 eV, and subsequent defect calculations were performed in supercells with fixed lattice parameters. The supercell size and k-point grid for the supercell are summarized in Table 1. All atomic positions and cell parameters were optimized until the residual forces on the relaxed atoms were within 0.02 eV $Å^{-1}$. Electronic density of states (DOS) were evaluated from calculations using the hybrid functional due to Heyd, Scuseria, and Ernzerhof[21] with a screening factor of 0.2 (HSE) as it provides significantly improved band gaps and band positions of semiconductors and insulators.[22,23] For these calculations, the k-point grids were 4×4×3 for the perovskites, 5×5×3 for La_2O_3 and La_2O_2S, and 1×4×2 for $La_2O_2SO_4$.

Table 1: Space group, supercell size and gamma centered k-point grid for the supercell according to the Monkhorst-Pack scheme.[24]

Material	Space group	Supercell	Atoms	k-points
La_2O_3	$P\bar{3}m1$	5×5×3	375	1×1×1
La_2O_2S	$P\bar{3}m1$	5×5×3	375	1×1×1
$La_2O_2SO_4$	$C2/c$	1×4×2	288	2×2×2
$SrZrO_3$				
$SrZrS_3$	$Pbnm$	3×3×2	360	2×2×2
$BaZrS_3$				

Defects were mainly considered in their fully ionized charge states by adjusting the total number of electrons in the system. The Gibbs formation energies of point defects were calculated from the total energy difference between defective and perfect supercells according to

$$\Delta G^{\mathrm{f}}_{\mathrm{defect}} = E^{\mathrm{tot}}_{\mathrm{defect}} - E^{\mathrm{tot}}_{\mathrm{perfect}} + \sum_i \Delta n_i \mu_i + q\mu_{\mathrm{e}} \quad (3)$$

where Δn_i is the number of constituent atoms exchanged upon defect formation, μ_i are the atomic chemical potentials, q is the effective charge state of the defect and μ_{e} is the Fermi level. The relative stability of different defects with the same charge can be evaluated independent of the Fermi level. Environmental conditions are defined through the temperature and pressure dependent chemical potential of gases obtained from

$$\mu_i(T, p_i) = \mu_i^{\circ} + k_{\mathrm{B}} T \, ln\left(\frac{p_i}{p^{\circ}}\right) \quad (4)$$

where the temperature dependency of μ_i° is obtained from thermochemical tables.[25] The chemical potential of oxygen is defined from the equilibrium between H_2O and H_2 in order to avoid using the O_2 molecule which is problematic within GGA,[26,27] and the same approach is taken for the chemical potential of sulfur

$$\mu_{\mathrm{O}} = \mu_{\mathrm{H_2O}} - \mu_{\mathrm{H_2}} \quad (5)$$

$$\mu_{\mathrm{S}} = \mu_{\mathrm{H_2S}} - \mu_{\mathrm{H_2}} \quad (6)$$

Equilibrium gas partial pressures for given conditions are obtained from a thermodynamic database[28] and inserted into Eqs. 4-6.

Proton migration barriers were calculated using the nudged elastic band (NEB) method. This approach has been applied for evaluating proton migration in several oxide systems.[29–37] The obtained energy barriers correspond to fully relaxed static barriers, meaning that the surrounding lattice is able to relax instantaneously around the proton throughout the migration event. As discussed by Hermet et al.[38], this relaxed lattice configuration may be close to the one observed during a proton migration event in a dynamic simulation which takes into account collective effects and the different time scales of motion for protons and the lattice ions, as well as proton tunneling. Proton migration barriers have also been shown to be underestimated in hydrogen-bonded systems within GGA.[39] Nevertheless, it is the relative differences in the proton migration barriers between the perovskite oxide and sulfides that are considered of most interest in the present work. The NEB calculations were performed with k-point sampling at the Γ-point only, resulting in energy barriers within 1-3 meV of selected calculations using a 2×2×2 k-point grid.

3. Results and discussion

3.1 Crystallographic and electronic structure

Figure 1 and Figure 2 show the relaxed structure of La_2O_3, La_2O_2S, and $La_2O_2SO_4$ and the perovskites, respectively. The relaxed structural parameters are summarized in Table 2 and found to be in good agreement with experimental values at room temperature, i.e., lattice parameters within 0.1-1.4 % and 0.1-0.8 %, respectively, for GGA and HSE type calculations.[40–44] As expected, the band gaps from GGA calculations are significantly underestimated compared to those obtained by HSE calculations (Table 2). Notably, the oxysulfide and sulfides exhibit considerably lower band gaps than their isostructural oxide counterparts. The band gaps from the HSE calculations were found to be in good agreement with available experimental estimates, e.g., 6 eV for La_2O_3,[45] 5.35 eV for La_2O_2S,[46] and 5.2 eV for $SrZrO_3$.[47]

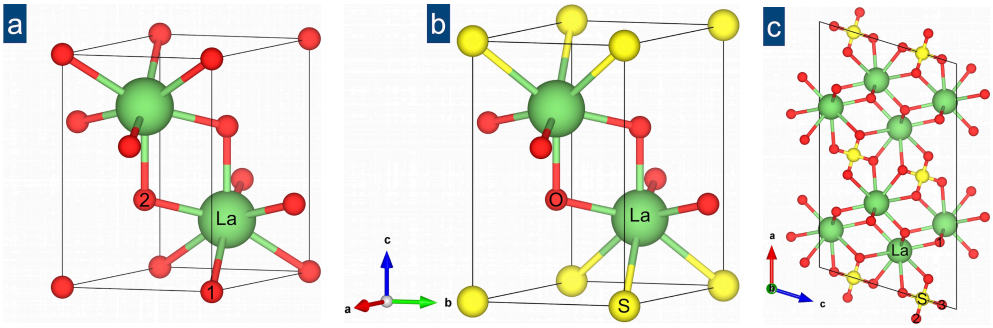

Figure 1: Relaxed structure of La_2O_3 (a), La_2O_2S (b) and $La_2O_2SO_4$ (c). In La_2O_3, the O1 and O2 sites are the 1a and 2d Wyckoff positions, respectively. $La_2O_2SO_4$ contains an isolated O-site and two O-sites in the SO_4 group, all in the 8f Wyckoff symmetry.

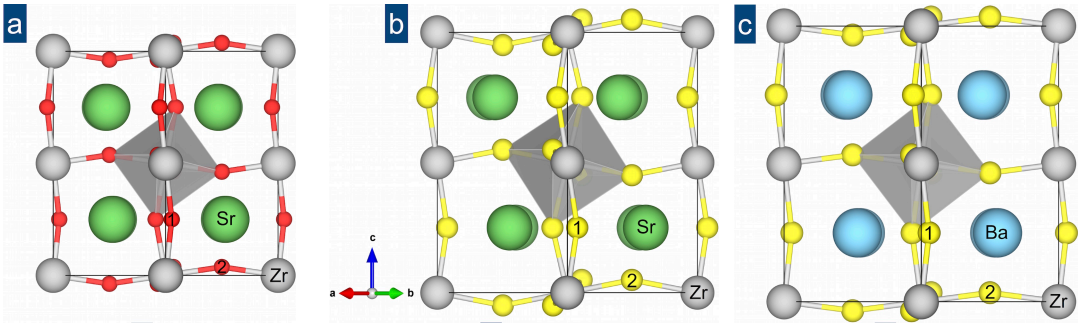

Figure 2: Relaxed structure of $SrZrO_3$ (a), $SrZrS_3$ (b) and $BaZrS_3$ (c). The degree of octahedral tilting is most similar between $SrZrO_3$ and $BaZrS_3$. The anion sites denoted 1 and 2 are the 4c and 8d Wyckoff positions, respectively.

Table 2: Relaxed lattice parameters and band gap from GGA/HSE calculations. The perovskite sulfides exhibited direct band gaps. The β angle for $La_2O_2SO_4$ was 107.19/107.16 ° compared to the experimental value of 107.0 °.[42]

Material	**Lattice parameters**			**Band gap**
	a / Å	*b* / Å	*c* / Å	eV
La_2O_3	3.93 / 3.91	–	6.16 / 6.10	4.02 / 5.54
La_2O_2S	4.06 / 4.03	–	6.95 / 6.91	3.14 / 4.39
$La_2O_2SO_4$	14.43 / 14.33	4.30 / 4.27	8.42 / 8.35	4.79 / 6.95
$SrZrO_3$	5.81 / 5.78	5.87 / 5.82	8.24 / 8.19	3.73 / 5.34
$SrZrS_3$	6.79 / 6.75	7.16 / 7.13	9.84 / 9.79	1.23 / 2.04
$BaZrS_3$	7.06 / 7.03	7.16 / 7.12	10.04 / 10.00	1.05 / 1.82

The site projected DOS of La_2O_3, La_2O_2S and $La_2O_2SO_4$ are shown in Figure 3. The valence band of La_2O_3 consists primarily of O 2p states while the valence band of La_2O_2S consists of O 2p and S 3p states with the latter located at slightly higher energy. In the case of $La_2O_2SO_4$, the valence band consists mainly of O 2p states of the regular oxide ions. The S and O states of the sulfate group are located at lower energy, indicating that oxygen vacancies are preferred on the regular oxide ion site rather than in the sulfate group.

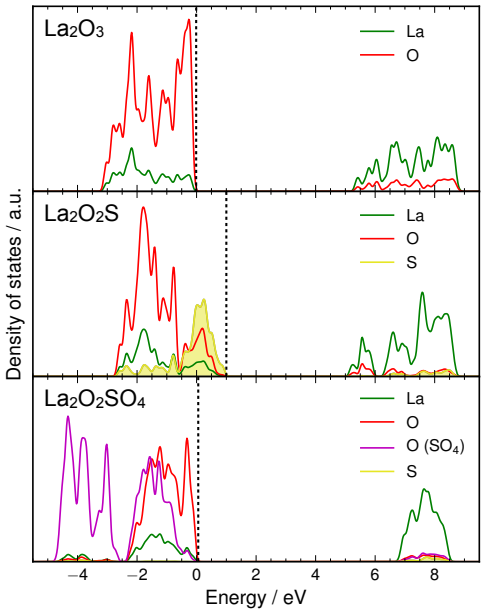

Figure 3 Site projected DOS for La_2O_3 (top), La_2O_2S (middle) and $La_2O_2SO_4$ (bottom). The valence band maximum (dashed lines) of La_2O_3 is referenced to 0 eV, and the Zr 4s states (not shown) are aligned between the materials.

Figure 4 shows the site projected DOS of the perovskite oxide and sulfides, which exhibit rather similar characteristics apart from the significant difference in band gap (Table 2). In general, the electronic structure of the oxides exhibit somewhat sharper peaks indicative of states that are more distinct and ionic in nature compared to the sulfides and oxysulfide, as previously reported for $BaZrS_3$.[48]

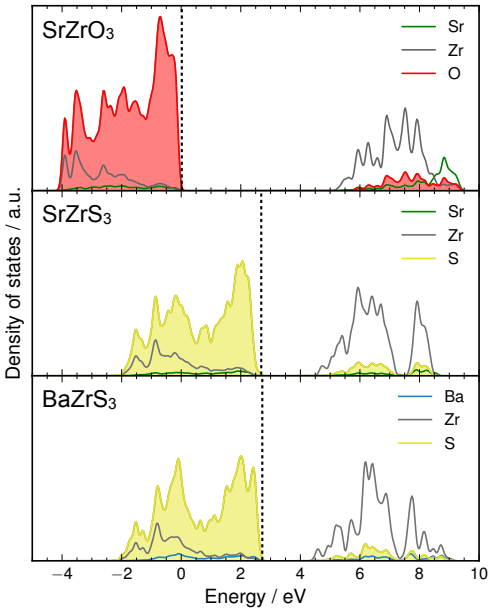

Figure 4: Site projected DOS for $SrZrO_3$ (top), $SrZrS_3$ (middle) and $BaZrS_3$ (bottom). The valence band maximum of $SrZrO_3$ (dashed lines) is referenced to 0 eV, and the La 5s states (not shown) are aligned between the materials.

The thermodynamic stability of $BaZrS_3$ and $SrZrS_3$ can be estimated based on the enthalpies of reaction between the respective oxides and H_2S, e.g., according to

$$BaZrO_3 + 3H_2S(g) = BaZrS_3 + 3H_2O(g) \quad (7)$$

These enthalpies were found to be quite endothermic at 0.56 and 0.84 eV for $BaZrS_3$ and $SrZrS_3$, respectively, based on HSE type calculations. The perovskite sulfides were estimated

to be stable for p_{H_2S}/p_{H_2O} ratios of the order of 10^{20} and 10^{40} at 1073 K and 523 K, respectively. Reports on the synthesis of $BaZrS_3$, $SrZrS_3$ and similar perovskite sulfides therefore involve quite severe conditions such as firing alkaline-earth carbonates and transition-metal dioxides in a stream of H_2S in carbon crucibles,[44] or reaction of the ternary oxide with CS_2-saturated Ar in carbon crucibles,[49] at up to 1373 K in both cases.

The calculated reaction enthalpy of a corresponding reaction for formation of La_2O_2S, i.e.,

$$La_2O_3 + H_2S(g) = La_2O_2S + H_2O(g) \quad (8)$$

was found to be quite exothermic, -1.14 eV. La_2O_2S can be prepared by heat treating $La_2O_2SO_4$ in inert gas with a few percent H_2 and H_2S at 1273 K.[50]

3.2 Defect thermodynamics

In order to evaluate the predominant reaction for proton incorporation in the considered materials, the most stable proton sites and type of anion vacancies must be determined. Subsequently, the enthalpies of Reactions 1 and 2 can be evaluated for the most stable defect configurations.

3.2.1 Anion vacancies

The stability of oxygen vacancies in La_2O_3 was found to be more stable on the O2 site by 0.41 eV as compared to the O1 site. For La_2O_2S, the relative thermodynamic stability of sulfide and oxide ion vacancies must be compared for defined chemical potentials of oxygen and sulfur. At 800 K, the Gibbs formation energy of $v_O^{\bullet\bullet}$ is 0.56 eV lower than for $v_S^{\bullet\bullet}$ when p_{H_2O} and p_{H_2S} are the same (constant p_{H_2}), and the stability of $v_O^{\bullet\bullet}$ and $v_S^{\bullet\bullet}$ become equivalent for, e.g., 3×10^{-5} bar H_2S and 0.1 bar H_2O. Furthermore, $v_O^{\bullet\bullet}$ is favored at lower temperatures by approx. 0.1 eV per 100 K due to the different temperature dependence of the chemical potential of H_2O and H_2S. In $La_2O_2SO_4$, $v_O^{\bullet\bullet}$ was found to be more stable on the isolated O1 site by 2.4 eV relative to the two inequivalent O-sites in the SO_4-group. Although slightly more stable, an oxygen vacancy in the form of a pyrophosphate group, $(S_2O_7)_{2SO_4}^{\bullet\bullet}$, was still 2 eV higher in energy relative to the O1 site. However, entire sulfate group vacancies, $v_{SO_4}^{\bullet\bullet}$, was found to be the most stable anion vacancy by several eV per defect, even under oxidizing conditions such as air with 1% H_2S at 500 K. The Gibbs formation energy of $v_{SO_4}^{\bullet\bullet}$ is highly dependent on the oxygen chemical potential due to the large oxygen content of the sulfate group. For the perovskites, the stabilities of $v_O^{\bullet\bullet}$ and $v_S^{\bullet\bullet}$ were found to be quite similar on the 4c and 8d sites, i.e., within 2 meV for $SrZrO_3$ and 60-62 meV for the sulfides.

3.2.2 Protons

The stability of protons associated with the different anions in the La_2O_3, La_2O_2S and $La_2O_2SO_4$, as well as in different structural orientations, was found to exhibit rather large variations. In La_2O_3, protons were more stable associated with the O1 oxide ion by 0.60 eV with coordinates (x=0.18, y=0.09, z=0.11). In La_2O_2S, the proton was more stable associated with the oxide ion compared to the sulfide ion by 0.56 eV with coordinates (x=0.66, y=0.33, z=0.20), and the energy difference between various positions around the oxide ion was up to 0.52 eV. In $La_2O_2SO_4$, the proton was found to be most stable associated with the isolated O1 oxide ion with coordinates (x=0.32, y=0.48, z=0.32) and was up to 0.86 eV higher associated with the sulfate group oxide ions. The interaction energy between $PO_{4\,SO_4}^{\prime}$ and a proton associated with the PO_4 group was calculated to be 0.15 eV, i.e., non-binding. On a general basis, this may indicate that phosphates are suitable as acceptor dopants to introduce proton conduction in sulfates.

For the perovskites, the proton was found to be most stable associated with the O2/S2 anion by 0.22-0.44 eV over the O1/S1 anions. The relaxed O-H and S-H bond lengths in the most stable configurations were consistently 0.99-1.00 Å and 1.36-1.39 Å, respectively, in all materials. The effectively positive charge state of hydrogen was ensured for the lowest band gap sulfide ($BaZrS_3$), i.e., $H_i^{\times}$ dissociated to $SH_S^{\bullet}$ and a delocalized electron in the conduction band. This was also the case for the transition state from Section 3.3, where one otherwise may speculate whether proton-electron interaction can lower the proton migration barrier.

3.2.3 Enthalpies of proton incorporation

The enthalpies of the reactions in Eqs. 1 and 2, describing dissociative absorption of H_2O and H_2S, respectively, are summarized in Table 3 for the most stable defect sites described in the previous sections. All enthalpies are significantly exothermic meaning that the acceptor-doped materials can be predominated by protons as the charge-compensating defect up to intermediate temperature. $La_2O_2SO_4$ may be an exception due to its preference for sulfate ion vacancies and a viable proton incorporation reaction is uncertain. The calculated hydration enthalpy of $SrZrO_3$ corresponds well with previous DFT calculations, -1.05 to -1.25 eV,[51] and thermogravimetric studies, -1.10 eV.[52] Selected defect calculations were also performed for $BaZrS_3$ using the HSE functional (2×2×1 supercell, Γ-point sampling), and a resonable agreement was obtained for ΔH_2, -0.53 eV compared to -0.58 eV in Table 3. The difference of 0.05 eV between PBE and HSE based calculations can be considered rather small and can partly be attributed to the different cell sizes and corresponding difference in spurious interactions between the periodic images of the defects.

Table 3: Enthalpies of the reactions in Eqs. 1 and 2 ($H_2O(g) + v_O^{\bullet\bullet} + O_O^{\times} = 2OH_O^{\bullet}$ and $H_2S(g) + v_S^{\bullet\bullet} + S_S^{\times} = 2SH_S^{\bullet}$, respectively) based on the most stable defect configurations described in Sections 3.2.1 and 3.2.2.

Material	ΔH_1 / eV	ΔH_2 / eV
La_2O_3	-0.86	–
La_2O_2S	-1.31	-0.90
$La_2O_2SO_4$	-1.21	–
$SrZrO_3$	-1.08	–
$SrZrS_3$	–	-0.86
$BaZrS_3$	–	-0.58

3.3 Proton migration

The considerable variation in the stability of protons on the different anion sites in La_2O_2S and $La_2O_2SO_4$, as well as the rather low symmetry of the protonated structures, signify that long-range proton transport would exhibit substantial activation energies and low mobilities in these materials. Extensive analysis of proton migration pathways and energy barriers were therefore not considered further. The perovskites exhibit a larger number of nearly equivalent proton sites with relatively small variations in energy. Proton migration barriers were considered for $SrZrO_3$, $SrZrS_3$ and $BaZrS_3$ along an interoctahedral jump and a rotational path for a proton in its lowest energy position associated with the 8d anion. The intraoctahedral path has been shown to be less favored in orthorhombic perovskites and was therefore not considered for the rather heavily distorted structures in the present work.[29,38] Figure 5 shows the calculated migration barriers, bond lengths and structural distortion for the interoctahedral path. In all cases, the interoctahedral transition state involves the proton being equidistant to the anion at the initial and final positions (which move towards each other) while the rest of the Zr-octahedra remain rather undistorted. The magnitude of the migration barriers may be associated with the jump distance relative to anion-proton bond length and the corresponding

displacement of the initial and final anions. $SrZrS_3$ exhibits the largest rhombohedral distortion and the proton jump distance is only slightly longer than for $SrZrO_3$ despite the rather large difference in lattice parameters (Table 2). $SrZrS_3$ further exhibits the longest proton bond length, $d_{S-H} = 1.39$ Å, which is elongated by 21 % in the transition state to 1.67 Å. In comparison, the proton bond length in $SrZrO_3$, $d_{O-H} = 1.00$ Å, is elongated by 25 % in the transition state to 1.25 Å, and the proton jump is accompanied by a larger displacement of the oxide ions (see Figure 5b). $BaZrS_3$ exhibits a significantly longer jump distance and a slightly shorter proton bond length compared to $SrZrS_3$, $d_{S-H} = 1.36$ Å. Thus, for $BaZrS_3$ the proton jump involves both a larger elongation of the transition state proton bond length (24 %) and a stronger distortion of the structure in terms of sulfide ion displacement.

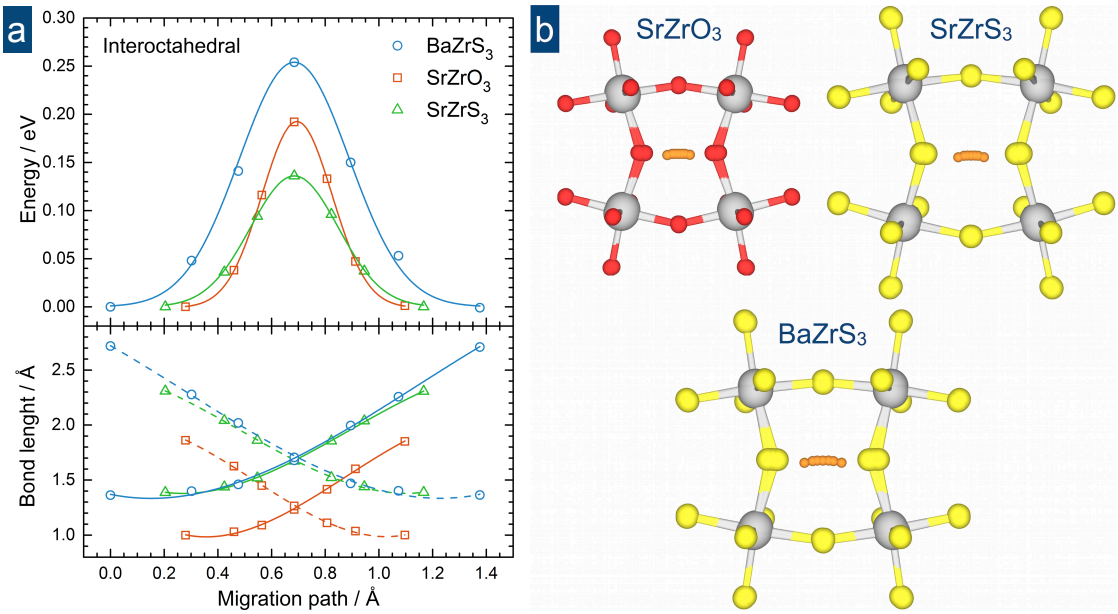

Figure 5: Proton migration barriers and bond lengths to the anions at the initial and final position of an interoctahedral jump (a), and superimposed images of the local structure around the migrating proton (b). The proton migration barriers amount to 0.14, 0.19 and 0.25 eV for $SrZrS_3$, $SrZrO_3$ and $BaZrS_3$, respectively. The energy profiles are fitted with a Gaussian function.

Figure 6 shows the calculated migration barriers, bond lengths and structural distortion for proton rotation around the 8d anion. The rotational path is asymmetric and the proton ends up in a higher energy position by 0.06, 0.15, and 0.07 eV for $SrZrO_3$, $SrZrS_3$, and $BaZrS_3$, respectively. The larger energy difference between the proton positions in the case of $SrZrS_3$ may be associated with the larger rhombohedral distortion and corresponding structural differences between the two 8d sulfide ion sites. Notably, the proton-anion bond length remains essentially constant throughout the rotation for all three materials (Figure 6b). The rotation brings the proton closer to the Sr/Ba cations and the steric repulsion leads to displacement of both the Sr/Ba cations and the OH/SH species (see Figure 6b), and the proton path curves too some extent to further increase the distance to the Sr/Ba cation. The lower energy barrier for proton rotation in the $BaZrS_3$ seems therefore to relate to the larger lattice volume and larger polarisability of Ba. For $SrZrO_3$ and $SrZrS_3$, the rotational barrier is higher than the interoctahedral barrier. The obtained rotational energy barrier for $SrZrO_3$ is somewhat larger than that obtained by a similar approach in smaller supercells, 0.22 eV.[33]

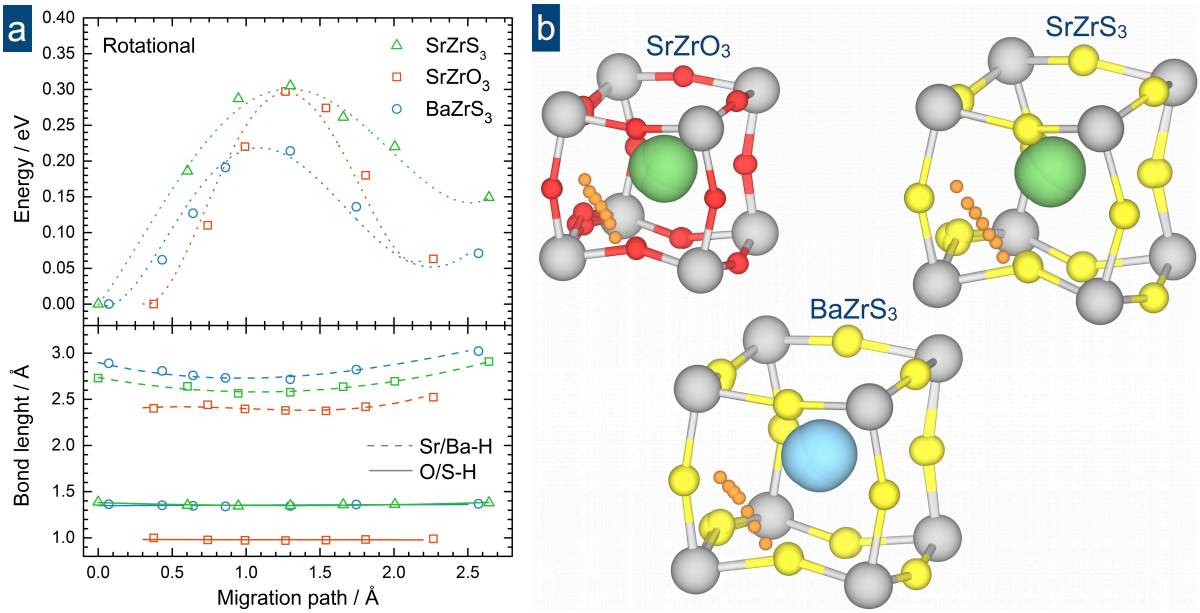

Figure 6: Proton migration barriers and bond lengths to the anion and Sr/Ba cation for a rotational path (a), and superimposed images of the local structure around the migrating proton (b). The proton migration barriers amount to 0.30, 0.30 and 0.21 eV for $SrZrS_3$, $SrZrO_3$ and $BaZrS_3$, respectively. The energy profiles are fitted with polynomial eye guides.

Based on the considered interoctahedral and rotational migration paths, $BaZrS_3$ exhibits the most favorable combination of energy barriers for long-range transport (0.25 and 0.21 eV). On the other hand, $BaZrS_3$ exhibits a less exothermic enthalpy of proton incorporation than the other perovskite sulfides (-0.58 eV, Table 3). In comparison to a state-of-the-art proton conducting oxide such as $BaZrO_3$, the theoretical migration barriers and hydration enthalpy are in the same range for the pristine material, i.e., 0.25-0.27 eV[29,33] and -(0.69-0.79) eV,[51,53,54] respectively. These values can be significantly influenced by the type and concentration of acceptor dopant as noted in several experimental and theoretical studies. The acceptor dopants can act as proton traps with binding energies exceeding the bulk migration barriers.[31,34,55–58] Trapping can thereby account for the higher activation energies observed experimentally, e.g., 0.43-0.48 eV for Y-doped $BaZrO_3$.[57,59,60] Experimentally obtained standard hydration enthalpies are also found to be somewhat more exothermic, e.g., -(0.77-0.86) eV for Y-doped $BaZrO_3$.[60–63]

The mobility of protons (like other ions) is enhanced by structure symmetry, which for perovskites can be represented by the Goldschmidt tolerance factor (0.95 for $BaZrS_3$). In this respect, the cubicity of $BaZrS_3$ may be increased by substituting smaller B-site cations such as Ga^{3+} as an acceptor dopant, or Ti^{4+} as long as the perovskite structure is kept from transitioning to the $BaNiO_3$-type structure of $BaTiS_3$.[49] Nevertheless, chemical stability is a decisive factor for the potential application of $BaZrS_3$ based materials as proton conducting ceramics, and it seems to be very limited in the presence of trace amounts of H_2O according to our calculations (Section 3.1). One may speculate whether $BaZrO_3$-$BaZrS_3$ exhibits solid solubility with O/S disorder and thermodynamic stability at lower p_{H_2S}/p_{H_2O} ratios than that required for the $BaZrS_3$ phase.

4. Conclusions

The enthalpies of dissociative absorption of H_2S or H_2O into anion vacancies in La_2O_2S, $SrZrS_3$ and $BaZrS_3$ imply that the acceptor doped materials can dissolve significant amounts of protons as $SH_S^{\bullet}$ in the sulfides or $OH_O^{\bullet}$ in La_2O_2S. For $La_2O_2SO_4$, the sulfate group vacancy was determined to be the energetically favored anion defect even under oxidizing conditions, and a prospective proton incorporation reaction is uncertain at this stage. For La_2O_2S, oxygen

vacancies were energetically favored over sulfide ions vacancies over a quite broad range of environmental conditions. By considering the symmetry of the protonated structures and variation in proton stability associated with the different anion sites, long-range proton transport can be expected to be slow in La_2O_2S and $La_2O_2SO_4$. A low binding energy between $PO_{4_{SO_4}}^{/}$ and a proton associated with the PO_4 group in $La_2O_2SO_4$ indicates that phosphates are suitable as acceptor dopants for proton conducting sulfates.

The calculated proton migration barriers of a selected interoctahedral and rotational path in perovskite $SrZrS_3$ and $BaZrS_3$ indicate that proton migration is comparable or more favorable in the sulfides than the isostructural oxide, $SrZrO_3$. The larger lattice volume of the perovskite sulfides, as well as a longer and relatively flexible S-H bond was found to facilitate proton migration. $BaZrS_3$ exhibited the most favorable combination of migration barriers, i.e., 0.25 and 0.21 eV for the interoctahedral and rotational barrier, respectively.

5. Acknowledgements

The Research Council of Norway is gratefully acknowledged for financial support under the project BioPCFC (219731) under the Nano2021 program. Computational resources were provided through The Norwegian Metacenter for Computational Science (NOTUR) under the project nn9259k. Dr. Nahum Masó (University of Oslo) is thanked for fruitful discussions.

6. References

(1) Dicks, A. L. Hydrogen Generation from Natural Gas for the Fuel Cell Systems of Tomorrow. *J. Power Sources* **1996**, *61*, 113–124.

(2) Gong, M.; Liu, X.; Trembly, J.; Johnson, C. Sulfur-Tolerant Anode Materials for Solid Oxide Fuel Cell Application. *J. Power Sources* **2007**, *168*, 289–298.

(3) Cheng, Z.; Wang, J.-H. J.; Choi, Y. Y.; Yang, L.; Lin, M. C.; Liu, M. From Ni-YSZ to Sulfur-Tolerant Anode Materials for SOFCs electrochemical Behavior, in Situ Characterization, Modeling, and Future Perspectives. *Energy Environ. Sci.* **2011**, *4*, 4380–4409.

(4) Aguilar, L.; Zha, S.; Cheng, Z.; Winnick, J.; Liu, M. A Solid Oxide Fuel Cell Operating on Hydrogen Sulfide (H_2S) and Sulfur-Containing Fuels. *J. Power Sources* **2004**, *135*, 17–24.

(5) Kröger, F. A.; Vink, H. J. Relations between the Concentrations of Imperfections in Crystalline Solids. *Solid State Phys. - Adv. Res. Appl.* **1956**, *3*, 307–435.

(6) Polfus, J. M.; Haugsrud, R. Protons in Perovskite Nitrides and Oxide Nitrides: A First Principles Study of $ThTaN_3$ and $SrTaO_2N$. *Solid State Commun.* **2012**, *152*, 1921–1923.

(7) Norby, T. Proton Conduction in Ca- and Sr-Substituted $LaPO_4$. *Solid State Ionics* **1995**, *77*, 240–243.

(8) Norby, T. Solid-State Protonic Conductors: Principles, Properties, Progress and Prospects. *Solid State Ionics* **1999**, *125*, 1–11.

(9) Amezawa, K.; Maekawa, H.; Tomii, Y.; Yamamoto, N. Protonic Conduction and Defect Structures in Sr-Doped $LaPO_4$. *Solid State Ionics* **2001**, *145*, 233–240.

(10) Amezawa, K.; Kitajima, Y.; Tomii, Y.; Yamamoto, N.; Widerøe, M.; Norby, T. Protonic Conduction in Acceptor-Doped LaP_3O_9. *Solid State Ionics* **2005**, *176*, 2867–2870.

(11) Toyoura, K.; Hatada, N.; Nose, Y.; Tanaka, I.; Matsunaga, K.; Uda, T. Proton-Conducting Network in Lanthanum Orthophosphate. *J. Phys. Chem. C* **2012**, *116*, 19117–19124.

(12) Haile, S. M.; Lentz, G.; Kreuer, K.-D.; Maier, J. Superprotonic Conductivity in $Cs_3(HSO_4)_2(H_2PO_4)$. *Solid State Ionics* **1995**, *77*, 128–134.

(13) Haile, S. M.; Calkins, P. M.; Boysen, D. Superprotonic Conductivity in β-$Cs_3(HSO_4)_2$ ($HX(P,S)O_4$). *Solid State Ionics* **1997**, *97*, 145–151.

(14) Chisholm, C. R. I.; Haile, S. M. Superprotonic Behavior of Cs2(HSO4)(H2PO4) - a New Solid Acid in the $CsHSO_4$-CsH_2PO_4 System. *Solid State Ionics* **2000**, *136-137*, 229–241.

(15) Blöchl, P. E. Projector Augmented-Wave Method. *Phys. Rev. B* **1994**, *50*, 17953–17979.

(16) Kresse, G.; Joubert, D. From Ultrasoft Pseudopotentials to the Projector Augmented-Wave Method. *Phys. Rev. B* **1999**, *59*, 1758–1775.

(17) Kresse, G.; Hafner, J. Ab Initio Molecular Dynamics for Liquid Metals. *Phys. Rev. B* **1993**, *47*, 558–561.

(18) Kresse, G.; Hafner, J. Ab Initio Molecular-Dynamics Simulation of the Liquid-Metal-Amorphous-Semiconductor Transition in Germanium. *Phys. Rev. B* **1994**, *49*, 14251–14269.

(19) Kresse, G. Efficiency of Ab-Initio Total Energy Calculations for Metals and Semiconductors Using a Plane-Wave Basis Set. *Comput. Mater. Sci.* **1996**, *6*, 15–50.

(20) Perdew, J.; Burke, K.; Ernzerhof, M. Generalized Gradient Approximation Made Simple. *Phys. Rev. Lett.* **1996**, *77*, 3865–3868.

(21) Heyd, J.; Scuseria, G. E.; Ernzerhof, M. Erratum: “Hybrid Functionals Based on a Screened Coulomb Potential” [J. Chem. Phys. 118, 8207 (2003)]. *J. Chem. Phys.* **2006**, *124*, 219906.

(22) Paier, J.; Marsman, M.; Hummer, K.; Kresse, G.; Gerber, I. C.; Angyán, J. G. Screened Hybrid Density Functionals Applied to Solids. *J. Chem. Phys.* **2006**, *124*, 154709.

(23) Alkauskas, A.; Broqvist, P.; Pasquarello, A. Defect Levels through Hybrid Density Functionals: Insights and Applications. *Phys. Status Solidi* **2011**, *248*, 775–789.

(24) Monkhorst, H. J.; Pack, J. D. Special Points for Brillouin-Zone Integrations. *Phys. Rev.*

B **1976**, *13*, 5188–5192.

(25) Chase, M. NIST-JANAF Thermochemical Tables, 4th Edition. *J. Phys. Chem. Ref. Data* **1998**, *Monograph*, 1952.

(26) Batyrev, I.; Alavi, A.; Finnis, M. Equilibrium and Adhesion of Nb/sapphire: The Effect of Oxygen Partial Pressure. *Phys. Rev. B* **2000**, *62*, 4698–4706.

(27) Meyer, B. First-Principles Study of the Polar O-Terminated ZnO Surface in Thermodynamic Equilibrium with Oxygen and Hydrogen. *Phys. Rev. B* **2004**, *69*, 045416.

(28) Bale, C. W.; Chartrand, P.; Degterov, S. A.; Eriksson, G.; Hack, K.; Ben Mahfoud, R.; Melançon, J.; Pelton, A. D.; Petersen, S. FactSage Thermochemical Software and Databases. *Calphad Comput. Coupling Phase Diagrams Thermochem.* **2002**, *26*, 189–228.

(29) Gomez, M. A.; Griffin, M. A.; Jindal, S.; Rule, K. D.; Cooper, V. R. The Effect of Octahedral Tilting on Proton Binding Sites and Transition States in Pseudo-Cubic Perovskite Oxides. *J. Chem. Phys.* **2005**, *123*, 0–10.

(30) Björketun, M.; Sundell, P.; Wahnström, G. Effect of Acceptor Dopants on the Proton Mobility in $BaZrO_3$: A Density Functional Investigation. *Phys. Rev. B* **2007**, *76*, 054307.

(31) Merinov, B.; Goddard, W. Proton Diffusion Pathways and Rates in Y-Doped $BaZrO_3$ Solid Oxide Electrolyte from Quantum Mechanics. *J. Chem. Phys.* **2009**, *130*, 194707.

(32) Fjeld, H.; Toyoura, K.; Haugsrud, R.; Norby, T. Proton Mobility through a Second Order Phase Transition: Theoretical and Experimental Study of $LaNbO_4$. *Phys. Chem. Chem. Phys.* **2010**, *12*, 10313–10319.

(33) Bork, N.; Bonanos, N.; Rossmeisl, J.; Vegge, T. Simple Descriptors for Proton-Conducting Perovskites from Density Functional Theory. *Phys. Rev. B - Condens. Matter Mater. Phys.* **2010**, *82*, 014103.

(34) Gomez, M. a.; Chunduru, M.; Chigweshe, L.; Foster, L.; Fensin, S. J.; Fletcher, K. M.; Fernandez, L. E. The Effect of Yttrium Dopant on the Proton Conduction Pathways of $BaZrO_3$, a Cubic Perovskite. *J. Chem. Phys.* **2010**, *132*, 0–8.

(35) Jeong, Y. C.; Kim, D. H.; Kim, B. K.; Kim, Y. C. Intra-Octahedral Proton Transfer in Bulk Orthorhombic Perovskite Barium Cerate. *Solid State Ionics* **2012**, *226*, 71–75.

(36) Kang, S. G.; Sholl, D. S. First Principles Studies of Proton Conduction in KTaO3. *J. Chem. Phys.* **2014**, *141*, 024707.

(37) Dawson, J. A.; Miller, J. A.; Tanaka, I. First-Principles Insight into the Hydration Ability and Proton Conduction of the Solid State Proton Conductor, Y and Sn Co-Doped $BaZrO_3$. *Chem. Mater.* **2015**, *27*, 901–908.

(38) Hermet, J.; Torrent, M.; Bottin, F.; Dezanneau, G.; Geneste, G. Hydrogen Diffusion in the Protonic Conductor $BaCe_{1-x}Gd_xO_{3-x/2}$ from Density Functional Theory. *Phys. Rev. B* **2013**, *87*, 104303.

(39) Barone, V.; Adamo, C. Proton Transfer in the Ground and Lowest Excited States of Malonaldehyde: A Comparative Density Functional and Post-Hartree–Fock Study. *J. Chem. Phys.* **1996**, *105*, 11007.

(40) Koehler, W. C.; Wollan, E. O. Neutron-Diffraction Study of the Structure of the A-Form of the Rare Earth Sesquioxides. *Acta Crystallogr.* **1953**, *6*, 741–742.

(41) Morosin, B. La2O2S Structure Refinement and Crystal Field. *Acta Crystallogr. Sect. B Struct. Crystallogr. Cryst. Chem.* **1973**, *29*, 2647–2648.

(42) Zhukov, S.; Yatsenko, A.; Chernyshev, V.; Trunov, V.; Tserkovnaya, E.; Antson, O.; Hölsä, J.; Baulés, P.; Schenk, H. Structural Study of Lanthanum Oxysulfate $(LaO)_2SO_4$. *Mater. Res. Bull.* **1997**, *32*, 43–50.

(43) Ahtee, A.; Ahtee, M.; Glazer, A. M.; Hewat, A. W. The Structure of Orthorhombic $SrZrO_3$ by Neutron Powder Diffraction. *Acta Crystallogr. Sect. B Struct. Crystallogr. Cryst. Chem.* **1976**, *32*, 3243–3246.

(44) Lelieveld, R.; Ijdo, D. J. W. Sulphides with the $GdFeO_3$ Structure. *Acta Crystallogr. Sect. B Struct. Crystallogr. Cryst. Chem.* **1980**, *36*, 2223–2226.

(45) Robertson, J. High Dielectric Constant Oxides. *Eur. Phys. J. Appl. Phys.* **2004**, *28*, 265–291.

(46) Dai, Q.; Song, H.; Wang, M.; Bai, X.; Dong, B.; Qin, R.; Qu, X.; Zhang, H. Size and Concentration Effects on the Photoluminescence of $La_2O_2S:Eu^{3+}$ Nanocrystals. *J. Phys. Chem. C* **2008**, *112*, 19399–19404.

(47) Zhang, A.; Lü, M.; Wang, S.; Zhou, G.; Wang, S.; Zhou, Y. Novel Photoluminescence of $SrZrO_3$ Nanocrystals Synthesized through a Facile Combustion Method. *J. Alloys Compd.* **2007**, *433*, L7–L11.

(48) Bennett, J. W.; Grinberg, I.; Rappe, A. M. Effect of Substituting of S for O: The Sulfide Perovskite $BaZrS_3$ Investigated with Density Functional Theory. *Phys. Rev. B - Condens. Matter Mater. Phys.* **2009**, *79*, 235115.

(49) Clearfield, A. The Synthesis and Crystal Structures of Some Alkaline Earth Titanium and Zirconium Sulfides. *Acta Crystallogr.* **1963**, *16*, 135–142.

(50) Haynes, J. W.; Brown, J. J. Preparation and Luminescence of Selected Eu^{3+}-Activated Rare Earth-Oxygen-Sulfur Compounds. *J. Electrochem. Soc.* **1968**, *115*, 1060.

(51) Bjørheim, T. S.; Kuwabara, A.; Ahmed, I.; Haugsrud, R.; Stølen, S.; Norby, T. A Combined Conductivity and DFT Study of Protons in $PbZrO_3$ and Alkaline Earth Zirconate Perovskites. *Solid State Ionics* **2010**, *181*, 130–137.

(52) Krug, F.; Schober, T. The High-Temperature Proton Conductor Strontium Zirconate: Thermogravimetry of Water Uptake. *J. Am. Ceram. Soc.* **1997**, *80*, 794–796.

(53) Björketun, M. E.; Sundell, P. G.; Wahnström, G. Structure and Thermodynamic Stability of Hydrogen Interstitials in $BaZrO_3$ Perovskite Oxide from Density Functional Calculations. *Faraday Discuss.* **2007**, *134*, 247.

(54) Polfus, J. M.; Bjørheim, T. S.; Norby, T.; Haugsrud, R. Nitrogen Defects in Wide Band Gap Oxides: Defect Equilibria and Electronic Structure from First Principles Calculations. *Phys. Chem. Chem. Phys.* **2012**, *14*, 11808–11815.

(55) Sundell, P. G.; Björketun, M. E.; Wahnström, G. Thermodynamics of Doping and Vacancy Formation in $BaZrO_3$ Perovskite Oxide from Density Functional Calculations. *Phys. Rev. B* **2006**, *73*, 104112.

(56) Stokes, S. J.; Islam, M. S. Defect Chemistry and Proton-Dopant Association in $BaZrO_3$ and $BaPrO_3$. **2010**, 6258–6264.

(57) Yamazaki, Y.; Blanc, F.; Okuyama, Y.; Buannic, L.; Lucio-Vega, J. C.; Grey, C. P.; Haile, S. M. Proton Trapping in Yttrium-Doped Barium Zirconate. *Nat. Mater.* **2013**, *12*, 647–651.

(58) Dawson, J. A.; Tanaka, I. Proton Trapping in Y and Sn Co-Doped $BaZrO_3$. *J. Mater. Chem. A* **2015**, *3*, 10045–10051.

(59) Bohn, H. G.; Schober, T. Electrical Conductivity of the High-Temperature Proton Conductor $BaZr_{0.9}Y_{0.1}O_{2.95}$. *J. Am. Ceram. Soc.* **2000**, *83*, 768–772.

(60) Kreuer, K. D.; Adams, S.; Münch, W.; Fuchs, a.; Klock, U.; Maier, J. Proton Conducting Alkaline Earth Zirconates and Titanates for High Drain Electrochemical Applications. *Solid State Ionics* **2001**, *145*, 295–306.

(61) Schober, T.; Bohn, H. G. Water Vapor Solubility and Electrochemical Characterization of the. *Solid State Ionics* **2000**, *127*, 351–360.

(62) Ricote, S.; Bonanos, N.; Caboche, G. Water Vapour Solubility and Conductivity Study of the Proton Conductor $BaCe_{0.9-x}ZrxY_{0.1}O_{3-\delta}$. *Solid State Ionics* **2009**, *180*, 990–997.

(63) Kjølseth, C.; Wang, L. Y.; Haugsrud, R.; Norby, T. Determination of the Enthalpy of Hydration of Oxygen Vacancies in Y-Doped $BaZrO_3$ and $BaCeO_3$ by TG-DSC. *Solid State Ionics* **2010**, *181*, 1740–1745.

TOC Graphic

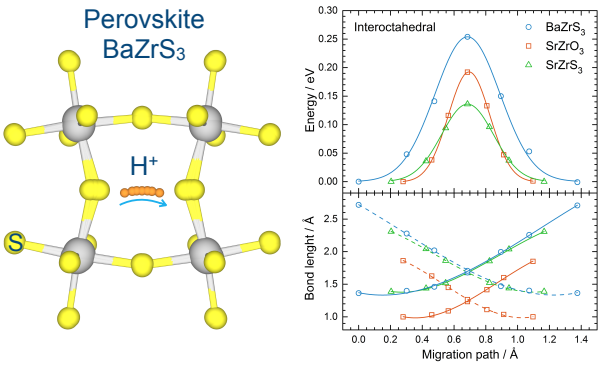
Perovskite
BaZrS3
H+
S
Interoctahedral
BaZrS3
SrZrO3
SrZrS3
Energy / eV
Bond lenght / Å
Migration path / Å